



# 1 Slow build-up of turbidity currents triggered by a moderate 2 earthquake in the Sea of Marmara

3

4 Pierre Henry<sup>1</sup>, M Sinan Özeren<sup>2</sup>, Nurettin Yakupoğlu<sup>3</sup>, Ziyadin Çakır<sup>3</sup>, Emmanuel de  
 5 Saint-Léger<sup>4</sup>, Olivier Desprez de Gésincourt<sup>4</sup>, Anders Tengberg<sup>5</sup>, Cristele Chevalier<sup>6</sup>,  
 6 Christos Papoutsellis<sup>1</sup>, Nazmi Postacıoğlu<sup>7</sup>, Uğur Dogan<sup>8</sup>, Hayrullah Karabulut<sup>9</sup>,  
 7 Gülsen Uçarkuş<sup>3</sup>, M Namık Çağatay<sup>3</sup>

8

9 <sup>1</sup>Aix Marseille Univ, CNRS, IRD, INRAE, Coll France, CEREGE, Aix-en-Provence,  
 10 France, <sup>2</sup>Istanbul Technical University, Eurasia Institute of Earth Sciences, Maslak,  
 11 Istanbul, Turkey, <sup>3</sup>Istanbul Technical University, Geological Engineering Dept.,  
 12 Maslak, Istanbul, Turkey, <sup>4</sup>CNRS, DT INSU, Parc national d'instrumentation  
 13 océanographique, Plouzané, France, <sup>5</sup>Aanderaa Data Instruments AS, Bergen,  
 14 Norway, <sup>6</sup>Aix Marseille Univ, CNRS, IRD, MIO, Aix-en-Provence, France, <sup>7</sup>Istanbul  
 15 Technical University, Physics Dept., Maslak, Istanbul, Turkey, <sup>8</sup>Yıldız Technical  
 16 University, Geomatic Engineering Dept., Istanbul, Turkey, <sup>9</sup>Bogazici University,  
 17 KOERI, Istanbul, Turkey

18

19 *Correspondence to:* Pierre Henry (henry@cerege.fr)

20

21 **Abstract.** Earthquake-induced submarine slope destabilization is known to cause  
 22 debris flows and turbidity currents, but the hydrodynamic processes associated with  
 23 these events remain poorly understood. Records are scarce and this notably limits  
 24 our ability to interpret marine paleoseismological sedimentary records. An  
 25 instrumented frame comprising a pressure recorder and a Doppler recording current  
 26 meter deployed at the seafloor in the Sea of Marmara Central Basin recorded  
 27 consequences of a  $M_w = 5.8$  earthquake occurring Sept 26, 2019 and of a  $M_w = 4.7$   
 28 foreshock two days before. The smaller event caused sediment resuspension but no  
 29 strong current. The larger event triggered a complex response involving a mud flow  
 30 and turbidity currents with variable velocities and orientations, which may result from  
 31 multiple slope failures. A long delay of 10 hours is observed between the earthquake  
 32 and the passing of the strongest turbidity current. The distance travelled by the  
 33 sediment particles during the event is estimated to several kilometres, which could



account for a local deposit on a sediment fan at the outlet of a canyon, but not for the covering of the whole basin floor. We show that after a moderate earthquake, delayed turbidity current initiation may occur, possibly by ignition of a cloud of resuspended sediment. Some caution is thus required when tying seismoturbidites with earthquakes of historical importance. However, the horizontal extent of the deposits should remain indicative of the size of the earthquake.

## 1. Introduction

Triggering of mass flows and turbidity currents by earthquakes is a hazard that can damage infrastructure at the seafloor (Heezen et al., 1954) and may enhance coseismic tsunami generation (Okal and Synolakis, 2001; Synolakis et al., 2002; Hebert et al., 2005; Ozeren et al., 2010). It is often considered that a peak ground acceleration (PGA) of the order of 0.1 g is needed for an earthquake to trigger a submarine slope instability (Dan et al., 2008; Nakajima and Kanai, 2000). However, a global compilation of cable breaks shows that, exceptionally, mass flow have been triggered by individual earthquakes of  $M_w$  as low as 3.1 (with  $PGA \approx 10^{-3} g$ ) and that, on the other hand many  $M_w > 7$  have failed to break cables, notably in zones (e.g. Japan Trench) where sediment input is relatively low and earthquakes frequent (Pope et al., 2016). In the Mediterranean region, the threshold is reportedly around  $M_w =$

In spite of this high regional variability, turbidite deposits in several seismically active zones have been used successfully as paleoseismological event markers (Goldfinger et al., 2003, 2012; McHugh et al., 2014; Ikehara et al., 2016). This requires distinguishing between seismoturbidites, caused by earthquakes and related mass wasting events, from those resulting from other processes (e.g. floods, storms, sediment loading). Seismoturbidites are generally described as turbidite-homogenites where a basal silt-sand bearing layer is overlaid by a layer of apparently homogenous mud with small or gradual, if any, variations in grain size and chemical composition (Polonia et al., 2013; McHugh et al., 2011; Çağatay et al. 2012; Eriş et al., 2012; Gutierrez-Pastor et al., 2013; Beck et al., 2007). In lakes and closed basins several characteristics of deposits following earthquake or landslides, such as the sharp boundary between turbidite and homogenite layers, the alternation of silt/sand and mud laminae within a single turbidite-homogenite unit and presence of bi-directional cross- or flaser- bedding have been interpreted as indicators of deposition from oscillatory currents associated with seiches or turbidity current reflection (Beck et al.,

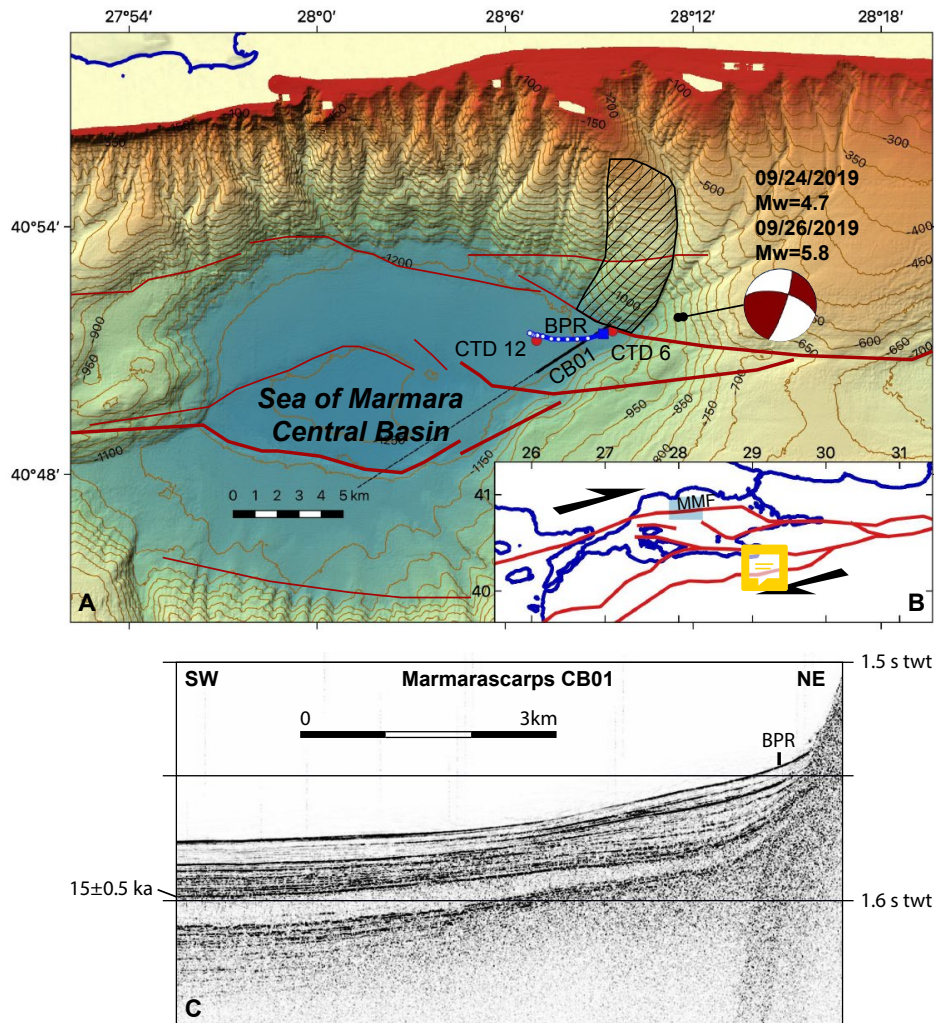


2007; Çağatay et al. 2012; McHugh et al., 2011). Seismoturbidites on ocean margins have fairly similar characteristics to those in closed basins but their layering has been interpreted differently, as a consequence of confluence (stacked or amalgamated turbidites) or current speed variations (multi-phased turbidites) (Gutierrez-Pastor et al., 2013; Nakajima and Kanai, 2000; Goldfinger et al., 2003). There is currently a lack of in situ records that could substantiate inferred hydrodynamic processes. Monitoring experiments brought records of ~~representative cases of~~ turbidity currents flowing in submarine canyons and initiated by ~~meteorological events~~ and occasionally by landslides (Azpiroz-Zabala et al., 2017; Khripounoff et al., 2012; Xu et al., 2004, 2010; Liu et al., 2012; Hughes Clarke, 2016). Oscillatory currents resulting from internal waves have been recorded after landslides in lakes (Brizuela et al., 2019). On the other hand, most information on earthquake-triggered events is still indirect based on cable ruptures (e.g. Pope, 2017; Hsu et al., 2008), combined with geomorphological and sedimentological observations (Cattaneo et al., 2012; Piper et al., 1999), and information from displaced instruments (Garfield et al., 1994). In Japan, in situ records of pressure and temperature were obtained from displaced OBSs after the Tohoku 2011  $M_w$  9.1 earthquake (Arai et al., 2013), and from cabled observatories after the Tokachi-Oki 2003  $M_w$  8.3 earthquake (Mikada et al., 2003) and after a moderate ( $M$  5.4) earthquake off Izu Peninsula (Kasaya et al., 2009). After the large events, strong currents of more than 1 m/s were implied starting 2-3 hours after the earthquake with no indication of oscillation or pulsing. In the off-Izu case a mudflow was observed with a camera 5 minutes after the earthquake and followed 15 minutes later by a change in current direction and speed.

We here present results from an instrumental deployment at the seafloor that accidentally recorded the consequences of earthquakes that occurred 09/24/2019 and 09/26/2019 in the Sea of Marmara with respective magnitudes 4.7 and 5.8 (Figure 1A). Holocene seismoturbidite records in the Sea of Marmara basins display a recurrence of 200 to 300 years, that roughly corresponds to the recurrence interval of  $M_w > 7$  earthquakes (McHugh et al., 2006, 2014; Drab et al., 2012, 2015; Yakupoğlu et al., 2018; Bulut et al., 2019). The pressure, temperature and current record from this single instrument demonstrate that this moderate earthquake triggered turbidity currents. However, the instrument suffered a rather complex sequence of disturbances and a 10 hours delay is observed between the earthquake and the recording of peak current.



100 We here propose a scenario which could explain the observations and discuss their  
101 implications for the understanding of seismoturbidite records.



102  
103 **Figure 1.** Context of instrumental deployment. (A) bathymetric map of the Sea of  
104 Marmara Central Basin with simplified fault geometry (in red). The hatched zone is a  
105 suspected mass wasting zone (Zitter et al., 2012). Location of instrumented frame  
106 comprising bottom pressure recorder (BPR) and doppler current meter is indicated by  
107 blue square. The blue banana with white dots represents the calculated trajectory of  
108 a sedimentary particle during the waning phase of the turbidity current. Red dots are  
109 CTD profiles 6 and 12 shown in supplementary material S1. Epicenter location of



110 earthquakes and the focal mechanism of the main shock are indicated. **(B)** Location  
 111 of study area. North Anatolian Fault system is shown in red. MMF is the Main  
 112 Marmara Fault. **(C)** Sediment sounder profile from Marmarascarp cruise (Armijo and  
 113 Malavieille, 2002). Indicative age of reflector from Beck et al. (2007). The instrument  
 114 (BPR) was deployed on a depositional fan at the base of slope and canyon outlet that  
 115 differ in character from the hemipelagite / turbidite-homogenite sequence in the  
 116 basin.

## 117 2. Context and data collection

118 A series of instrumental deployments was planned to record naturally occurring  
 119 resonant water column oscillations (seiches) at various locations in the Sea of  
 120 Marmara with the aim to improve tsunami models (Henry et al., 2021). An instrumented  
 121 frame was thus deployed at 40.8568° N, 28.1523° E and 1184 m water depth in the  
 122 Central Basin on May 9, 2019 and recovered 6 months later (11/19/2019) (Figure 1A).  
 123 This site is located at the outlet of a branched canyon system originating from the edge  
 124 of the continental shelf (Figure 1). Sediment ~~sounder~~ profiles indicate a depositional  
 125 fan or lobe is present at this location (Figure 1C). The short canyons observed on the  
 126 relatively steep sedimented slope ( $\approx 10^\circ$ ) of the Sea of Marmara deep basins are  
 127 presumably fed by instabilities of the canyon heads and walls (Zitter et al. 2012;  
 128 Çağatay et al., 2015). In addition, the slope west of the canyons immediately north of  
 129 the deployment site hosts a mass wasting feature covering about 24 km<sup>2</sup> (Zitter et al.  
 130 2012). The Main Marmara Fault (MMF, Figure 1B), is defined as the part of the northern  
 131 branch of the North Anatolian Fault system crossing the Sea of Marmara (Le Pichon  
 132 et al., 2001, 2003). A splay of the MMF runs along the base of this slope (Armijo et al.,  
 133 2002; Grall et al., 2012; Sengor et al., 2014). The 09/24/2019 and 09/26/2019  
 134 earthquakes occurred beneath the canyon system and their epicenters are located 5  
 135 km ENE of the instrument, less than 500 m apart (Figure 1). The rupture occurred within  
 136 the crust at 9-13 km depth on a northward dipping fault located north of principal  
 137 displacement zone of the Main Marmara Fault. The focal mechanism and aftershock  
 138 distribution indicate right-lateral strike-slip with a reverse component (Karabulut et al.,  
 139 2021). The rupture did not reach the seafloor, nor caused a tsunami. For instance, tidal  
 140 gauge records obtained at Marmara Ereğlisi do not deviate more than 1hPa from a  
 141 fitted tidal model.





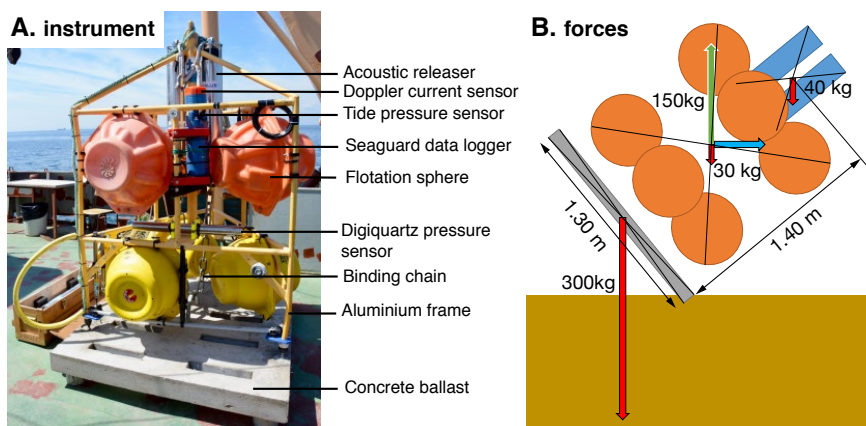
142 The instrumentation on the frame comprises (1) an RBR bottom pressure recorder  
143 (BPR) with a Paroscientific 0-2000 m Digiquartz sensor, (2) a Seaguard recording  
144 current meter (RCM) equipped with a Z-pulse 4520 Doppler current meter operating in  
145 the 1.9-2 MHz frequency range and other sensors: temperature, pressure (tide sensor  
146 Aanderaa 5217), conductivity (Aanderaa 4319), oxygen (Aanderaa optode 4330)  
147 (Figure 2). The RBR pressure recording interval was set to 5s and that of the Seaguard  
148 RCM to one hour for all sensors. The Doppler current meter worked in burst mode,  
149 averaging 150 pings taken every second at the end of each one-hour recording interval.  
150 The SeaGuard instrument was fixed on the upper part of the frame 1.5 m above the  
151 seafloor and emit 4 narrow (2°) beams at orthogonal directions in a plane, parallel to  
152 the seafloor if the frame is standing upright, and measures Doppler backscatter in cells  
153 extending 0.5-to-2 meters from the instrument (Figure 3). The instrument was set in  
154 forward ping mode, so that only data from sensors measuring a positive Doppler shift,  
155 upstream currents moving toward the instrument, are used to calculate current speed.  
156 The tide sensor is a piezoresistive sensor with a specified accuracy comparable to that  
157 of the Digiquartz sensors (4kPa for a 0-2000 m sensor vs. 2kPa for a Digiquartz sensor  
158 with the same range) and 0.2 hPa (2 mbar) resolution and comprises a temperature  
159 sensor of 0.2°C accuracy and 0.001°C resolution. The tide sensor averages pressure  
160 measured at a 2 Hz sampling rate over 300 s at the end of each one-hour time interval.  
161 the tide sensor was checked against an atmospheric reference between deployments  
162 and found to have a minimal drift, less than 1 hPa.

163 As we will show that the 09/24/2019 earthquake caused the instrumented device  
164 to lay on its side for several hours and then straighten up, understanding the setup of  
165 the seafloor device and its stability is important (Figure 2B). The frame is made of  
166 aluminium and has 6 rigidly bound flotation spheres of 25 kg buoyancy each. The net  
167 weight of the instrumented frame in water is 15 kg. The frame is rigidly attached to a  
168 12-cm-thick 1.5x1.3 m concrete slab, weighting 300 kg in water. The assembly of the  
169 heavy slab and buoyant frame is stable in upright position in the water and on the  
170 seafloor. Moreover, it is estimated that a current of 1 m/s would cause a total horizontal  
171 drag of 15 kg when the device is in upright position, which is insufficient to destabilize  
172 it. If a stronger current, or other external forces, cause the assembly to tilt and lay on  
173 one side, the moment of the gravity and buoyancy forces should straighten the device  
174 back to upright position when these external forces are removed.

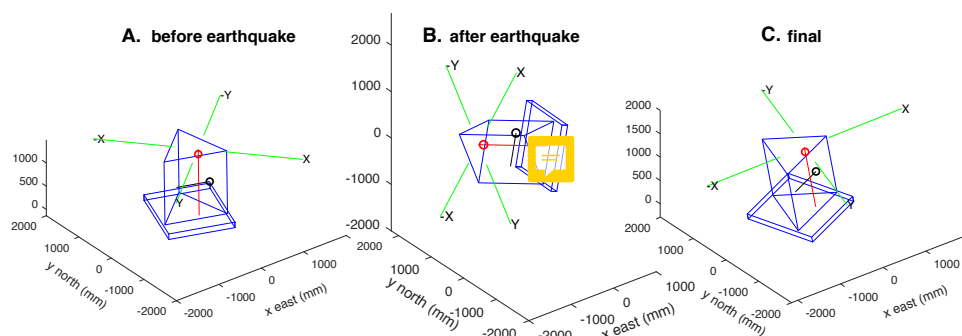


175 Measurement of current speed and direction by a tilted instrument is a related issue  
 176 that we here consider. The orientation and attitude of the Seaguard FGN is measured  
 177 with a 2-component accelerometer and a magnetic compass and the recorded data  
 178 include tilt in X and Y direction and the heading of the X axis. Tilt X and Y components  
 179 are factory calibrated from  $-35^\circ$  to  $+35^\circ$  with an accuracy of  $1.5^\circ$ . Tests performed in  
 180 the laboratory (see supplementary material, Figure S1) showed that tilt information  
 181 remains consistent outside this range, even when the instrument is upside down. Tilt  
 182 measurements are accurate within  $3^\circ$  up to  $60^\circ$  but saturate at about  $80^\circ$  (Figure S2).  
 183 Uncertainty on heading also increases with tilt, especially when the instrument is tilted  
 184 toward the X-direction. However, measured heading remains  $\pm 20^\circ$  of true heading for  
 185 a tilting of up to  $60^\circ$  (Figure S3). The current measured in the instrument plane is  
 186 corrected for tilt assuming current is horizontal. As far as this approximation is valid,  
 187 the current record should in principle remain fairly accurate when the instrument is  
 188 tilted beyond the normal range of operation ( $\pm 35^\circ$  degree) and at least to  $60^\circ$ . However,  
 189 the compass was not calibrated for an upside-down configuration. If the top of the  
 190 instrument would happen to be oriented downward, the measured current direction will  
 191 be unreliable, even though the absolute speed may still be correctly estimated. Another  
 192 problem may arise if one of the Doppler sensors is facing down into the sediment so  
 193 that its measurement cell is below the seafloor. If the sensor pointing upward in the  
 194 opposite direction is recording a negative Doppler shift, this value will be ignored in the  
 195 forward ping mode. In this case, the measurement retained to calculate current velocity  
 196 will correspond to noise from the sensor facing toward the seafloor. In all situations, it  
 197 remains possible to recalculate the sensor readings retained by the calculator from the  
 198 current velocity and orientation parameters recorded by the instrument, and thus  
 199 assess the reliability of data.

200



201  
 202 **Figure 2.** Instrumented frame. (A) photo of the instrumented frame before  
 203 deployment. (B) Sketch showing forces applied to the elements of the instrumented  
 204 frame in water. The red arrows represent the weight in water of the cement ballast, of  
 205 the instrumented frame and of the acoustic release system on top. The green arrow  
 206 represents the buoyancy of the flotation spheres. The blue arrow represents the  
 207 current drag, which depends on current speed and instrument tilt.  
 208  
 209



210  
 211 **Figure 3.** Reconstruction of frame position based on instrument tilt-meter and  
 212 compass data: (A) before the earthquake; (B) Tilted, between, 25 minutes and 10.5  
 213 hours after earthquake; (C) back in nearly upright position 11 hours after earthquake.  
 214 Position of Digiquartz pressure sensor (black circle), Aanderaa tide sensor (red  
 215 circle) and Doppler current meter beam cells (green segments)

216  
 217





## 218 3. Results and interpretations

### 219 3.1. Pressure and tilt records

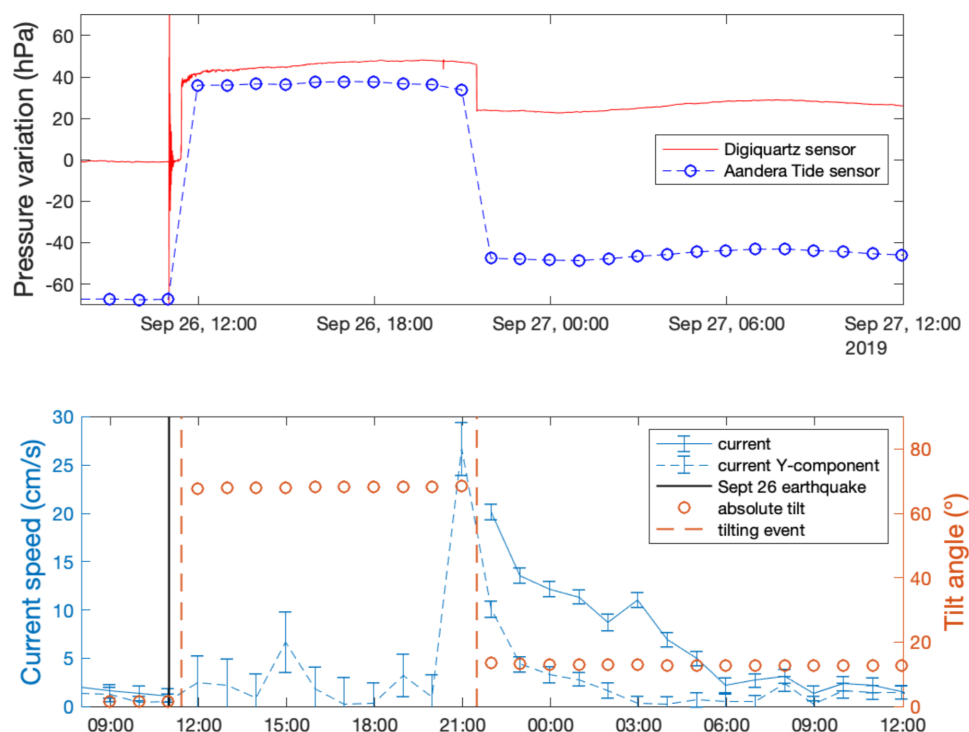
220 Pressure sensors are sensitive to pressure variations caused by P-waves and  
 221 Digiquartz sensors are also intrinsically sensitive to acceleration, but to a small extent,  
 222 160 hPa/g for an instrument with 20 MPa range according to the calibration report.  
 223 Small earthquakes are detected as pressure spikes, while oscillations are recorded  
 224 after large earthquakes. The  $M_w$  4.7 09/24/2019 caused a short pressure transient of  
 225 25 hPa at 08:00:26 followed by small pressure oscillations of less than 3 hPa amplitude  
 226 decaying over a few minutes. The seismic wave train from the  $M_w$  5.8, 09/26/1919  
 227 earthquake is recorded by the Digiquartz pressure sensor as oscillations, initiated by  
 228 a pressure drop of 65 hPa between 10:59:22 and 10:59:26 (Figure 4). For the sampling  
 229 interval of 5s used in this setup, the recorded signal is aliased, which precludes  
 230 quantitative interpretation in term of velocity or acceleration. However, the initial  
 231 pressure drop after the 09/26/1919 earthquake may indicate a negative polarity of the  
 232 first P arrival at the instrument site, located on an ascending ray-path.

233 Twenty-five minutes after the  $M_w$  5.8, earthquake, a new disturbance of the  
 234 pressure sensor is observed at 11:23:41. The pressure then progressively increases  
 235 by 30.9 hPa in 15 seconds between 11:24:46 and 11:25:01 before stabilizing. Over the  
 236 corresponding one-hour-time-interval between successive records, the Seaguard  
 237 RCM, initially subvertical (tilt less than  $2^\circ$ ), acquires a strong tilt (Figure 3). At 11:57:48,  
 238 measured tilt is  $-65^\circ$  along the X-axis and  $+19^\circ$  along the Y-axis, with X-axis in a  $N161^\circ$   
 239 azimuth and these values remain constant  $\pm 2^\circ$  over the next 10 hours, corresponding  
 240 to an absolute tilt of  $68^\circ$  (Figure 4). The tilting of the instrument causes the Digiquartz  
 241 and Tide sensors to record different pressure variations because they are located at  
 242 different positions on the frame (Figure 2). Moreover, the pressure readings by the  
 243 Digiquartz sensor also depend on its orientation relative to Earth gravity. Pressure at  
 244 the Tide sensor location increases about 100 kPa, corresponding to a 1 m drop and  
 245 indicating that the frame was then practically laying on its side. Ten hours later, the  
 246 device apparently straightens itself in about 5 seconds, between 21:28:29 and  
 247 21:28:34 as indicated by a rapid pressure variation. After that, the recorded tilt  
 248 parameters are moderate and stabilize at  $-11.5^\circ$  for the X-axis and  $5.3^\circ$  for the Y-axis,  
 249 with X-axis in a  $N105.3^\circ$  azimuth.



250 The  $M_w$  4.7 earthquake caused minor disturbances of the attitude of the  
 251 instrument, with variations of tilt and heading of less than  $0.5^\circ$ . A  $M_w$  3.6 foreshock of  
 252 the  $M_w$  5.8 occurring 26/09/2019 at 7:32 also caused minor disturbances. These  
 253 indicate that the seafloor was sensitive to ground shaking caused by these small  
 254 earthquakes, however, this did not cause the device to sink into the sediment. Changes  
 255 of pressure baseline of the digiquartz sensor between before and after these  
 256 earthquake are difficult to resolve, and correspond to less than 5 mm vertical  
 257 displacement for the first event and less than 2 mm for the second one.

258



259

260 **Figure 4.** Time series around the time of occurrence of a  $M_w$  5.8 earthquake; (top)  
 261 pressure variations recorded by two instruments on the instrumented frame; (bottom)  
 262 current and tilt data recorded by Seaguard RCM. Between the tilting events only one  
 263 component of the doppler current meter functioned reliably (Y-component oriented  
 264 N200) and is here reported.

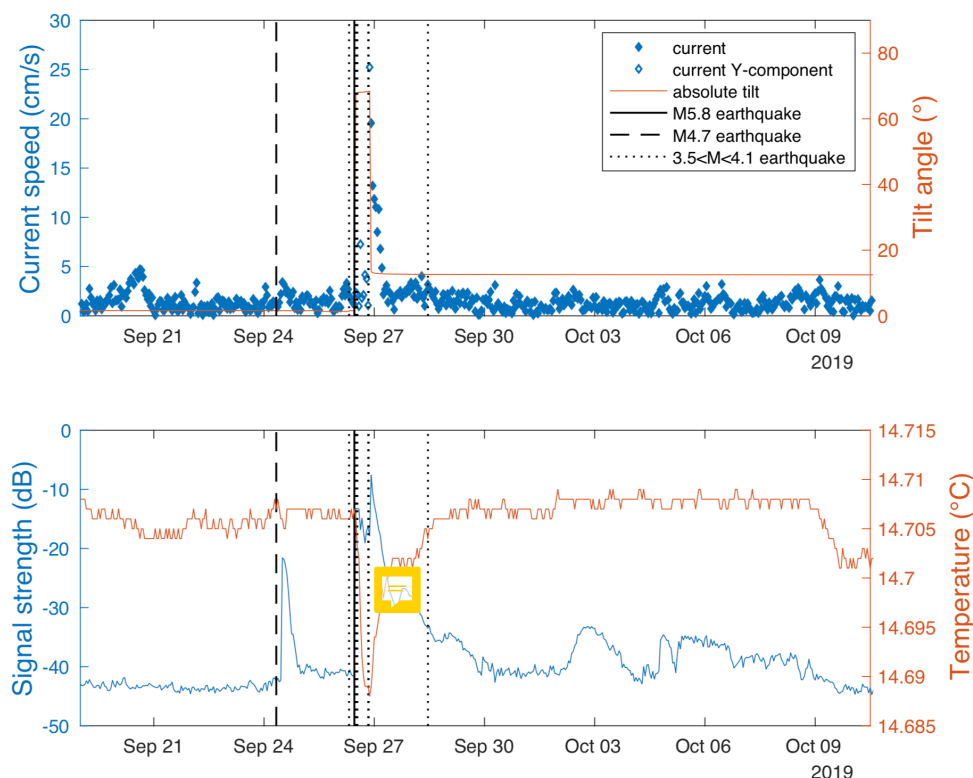


**Figure 5.** Time series acquired with Seaguard 30 M during the September 2019 seismicity cluster; (top) current speed and tilt; (bottom) backscatter signal strength and temperature.

### 3.2. Current records and possible causes of tilting

The  $M_w$  4.7 09/24/2019 earthquake was followed by a small increase of current strength peaking at 3.4 cm/s at noon, 4 hours after the earthquake (Figure 5). Comparable events in term of duration and strength occurred spontaneously 09/20/2019 (with currents up to 4.7 cm/s) and 09/26/2019 just before the main earthquake. During all three events the dominant current was from the east, thus coming from the direction of the canyon, but there is an important difference between the event that occurred after the earthquake and the two others. During that event a change in current direction occurred from eastward to westward between 10:57 and 11:57 while the current strength increased from 2.2 cm/s to its peak value (Figure 6). During the other events, build-up was more progressive and did not involve a change in direction. A drift plot, calculated by summing velocity vectors over time, reproduces



the motion of a particle assuming a uniform velocity field (Figure 6). The total drift is about 500 m and occurs in the 8 hours following the current inversion. Current direction varies from Westward to Northward during this time interval.

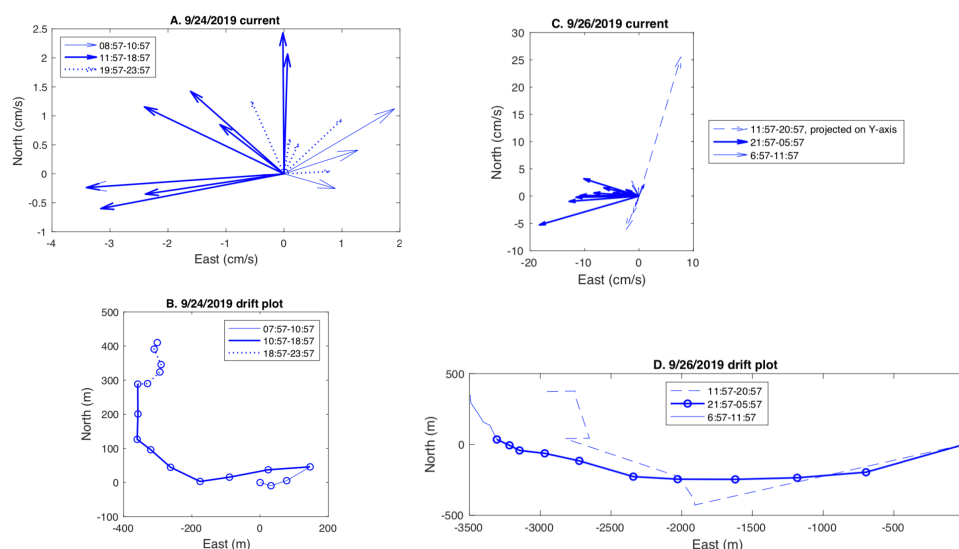


**Figure 6.** Current recorded after  $M_w$  4.7 and  $M_w$  5.8 earthquakes: (A) Current velocity arrows recorded every hour between 08:57 and 23:57 on 09/24/2019; (B) drift plot over the same time interval, the change of current direction and strength between 10:57 and 11:57 coincides with increasing backscatter strength (see figure 4), indicative of increased turbidity; (C) Current velocity arrows recorded every hour between 12:00 09/26/2019 and 06:00 09/27/2019. Dashed arrows show measurements acquired in the Y direction when the instrument was strongly tilted (position B in Figure 3), plain arrows when it was back in upright position (C in Figure 3); (D) drift plot over the same time interval, the dashed part corresponds to the strongly tilted position.

After the  $M_w$  5.8 09/26/2019 earthquake, during the 10 hours period when the instrument remained strongly tilted, the instrument recorded currents varying both in speed and orientation, but some precautions are needed when interpreting these data. The current component measured by transducers along the Y-axis of the instrument, oriented N  $20^\circ$ , probably remained accurate as the tilt along this axis is less than  $20^\circ$ .



304 and the measurement cell remained above the bottom (Figure 2B). On the other hand,  
 305 the X-component may not be reliable as one of the sensors ( $n^{\circ}1$ ) is oriented  $65^{\circ}$   
 306 upward in the  $N160^{\circ}$  direction, and the opposite sensor ( $n^{\circ}3$ ) is dipping  $65^{\circ}$  downward  
 307 in the opposite ( $N340^{\circ}$ ) direction. Consequently, measurement cell  $n^{\circ}3$  lies within the  
 308 sediment and thus may only record noise. Moreover, because the Doppler current  
 309 sensor (DCS) is set in forward pinging mode, current speed is calculated with data  
 310 from sensors measuring positive doppler shifts only. This implies that if the current  
 311 component toward  $N160^{\circ}$  is positive, sensor  $n^{\circ}1$  will measure a negative shift and will  
 312 not be recorded. During the time interval here considered, the measured current  
 313 component in the X-direction (toward  $N160$ ) is positive, which indicates that data from  
 314 sensor  $n^{\circ}4$  was used (Figure 7), and that is probably noise. It follows that the current  
 315 component along the Y-direction is the only one reliable. The horizontal current  
 316 measured along the Y-axis changed sign several times during this time interval, and  
 317 reached peak values of  $6.3 \text{ cm/s}$  toward  $N200$  at  $14:57:46$ , about four hours after the  
 318 earthquake, and of  $25 \text{ cm/s}$  in the opposite direction at  $20:57:46$ , the last measurement  
 319 before the instrument straightened up. Other measurements on both axes remain  
 320 below  $5 \text{ cm/s}$ , but the absolute velocity may have been higher because this  
 321 measurement was only performed in one direction. Yet, these observations suggest  
 322 that the strong current recorded before the instrument straightened up played a role  
 323 in this event. Once the device got back in an upright position, it recorded a current  
 324 consistently flowing westward and progressively decreasing from  $20 \text{ cm/s}$  to  
 325 background level ( $2 \text{ cm/s}$ ) in 9 hours (Figure 4). During this waning phase, the current  
 326 drift is about  $3.5 \text{ km}$  in a westward direction (Figure 6). The drift estimated during the  
 327 first 10 hours after the earthquake, while the instrument was strongly tilted, is in the  
 328 opposite direction but may not be reliable.

329

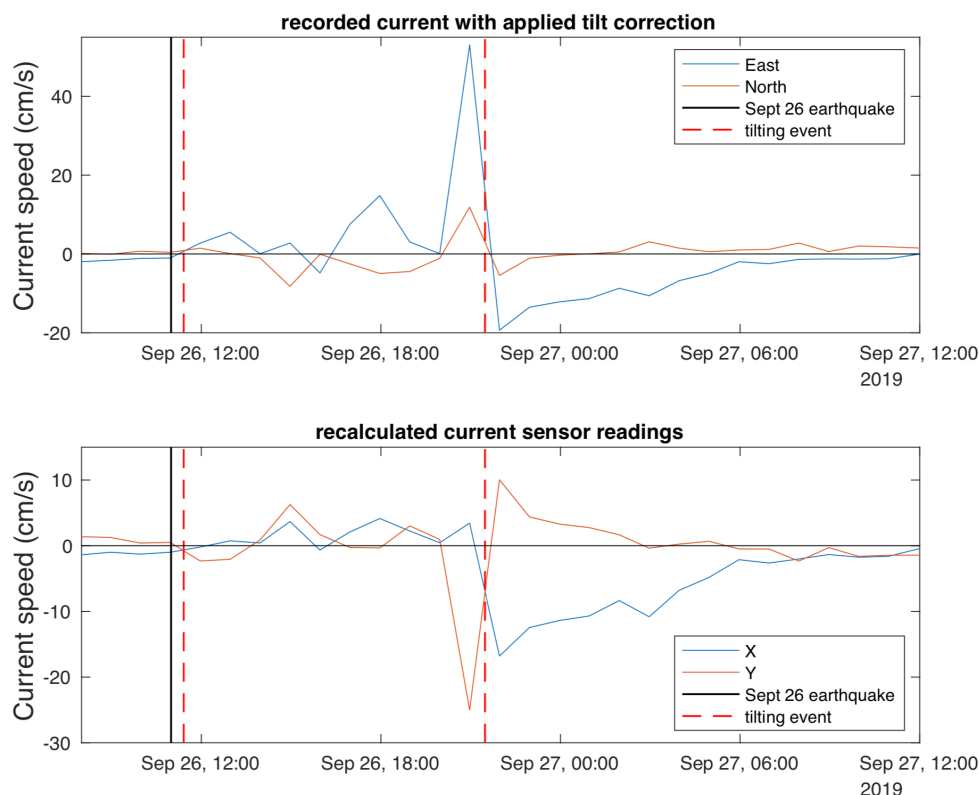


**Figure 7.** Current record acquired around the time of occurrence of a  $M_w$  5.8 earthquake. A. Instrumental record, automatically corrected for tilt at heading. B. recalculated readings in the X and Y axis of the Doppler sensor (see text for interpretation).

The current speed in the first 2 hours after the main earthquake apparently remained low, at most 5.6 cm/s. It is thus unlikely that the tilt of the device was caused by strong currents. Some short burst of current may have been missed because of the 1 hour sampling interval, but this would not explain why the frame then remained stable in a tilted position for several hours. Local liquefaction of the sediment beneath the device is also an unlikely cause because the tilting of the instrument occurred 25 minutes after the earthquake. A mud flow originating from the basin slopes thus appears as a more likely cause. This hypothesis would also account for the presence of sandy mud caked on the device in various places: on the frame feet, on the acoustic releasers, on the optode connector and also inside the plastic protection of a flotation





sphere, from which bindings were broken and had to be repaired. On the other hand, the current speed in the 20-50 cm/s range recorded before, as well as after, the time when the device straightened up is strong enough to cause erosion of mud or sand deposits. It may thus be hypothesized that erosion freed the device from the mud cover. The flotation spheres on the frame and the concrete ballast at its base exert a moment that should keep the assembly stable in an upright position unless the frame is loaded with sediment.

### 3.3. Acoustic backscatter record

The strength of the backscattered signal can be used as a proxy for turbidity. The Seaguard RCM emits in the 1.9-2 MHz band corresponding to a wavelength ( $\lambda$ ) of 750  $\mu\text{m}$ . Doppler backscatter current meters have maximum sensitivity for particles of diameter  $D = \lambda/\pi$  and can detect particles down to diameter  $D = 0.08 \lambda$ , for which backscatter power is less than 1/10 of peak backscatter power (Guerrero et al., 2011, 2012). The seaguard RCM should thus be mostly sensitive to the presence in suspension of sand size particles (larger than 63  $\mu\text{m}$ ). The background backscatter amplitude level is  $-43 \pm 1 \text{ dB}$  before the earthquakes. Three to four hours after the  $M_w$  4.7 09/24/2019 earthquake, backscatter increases sharply to  $-22 \text{ dB}$  between 11:00 and 12:00, and then decays to  $-41 \text{ dB}$  in 12 hours. The increase of backscatter coincides with a change of current direction and speed, indicating that the turbid cloud was brought to the instrument site by the current. However, the current speed of less than 4 cm/s may have been insufficient to put the particles in suspension. There is no increase of backscatter on Sept 20 when stronger currents coming from the same direction, but not related with an earthquake, were recorded.

Backscatter strength remain  $41 \pm 1 \text{ dB}$  the 1.5 days interval before the  $M_w$  5.8 09/26/2019 and increases to the  $-20 \text{ dB}$  to  $-13 \text{ dB}$  range after the earthquake (Figure 5), which implies sand sized sediment was put in suspension soon after the earthquake although the local current speed remained relatively low (about 5 cm/s at most). After the device went back to near vertical position, signal strength reaches a maximum of  $-7.6 \text{ dB}$ , which correspond to an amplitude ratio of 42 and an intensity ratio of 1800 compared to base level. Similar signal strength levels are typically reached with the Pulse sensor in highly turbid water such as in estuaries. During deep sea deployments signal strength range more typically between  $-60$  and  $-40 \text{ dB}$ . After reaching peak value,



backscattered signal strength progressively decays to stabilise at about -40 dB 3 days (Figure 5). Several turbid events, with signal strength about -35 dB are observed in October and associated with small increases in current velocity (up to 3-4 cm/s). It is unclear whether these passing clouds are residual turbidity from the earthquake. After October 9, backscatter eventually returns to background level while temperature decreases by 0.007 °C over a few hours, indicating replacement of the water mass around the instrument.

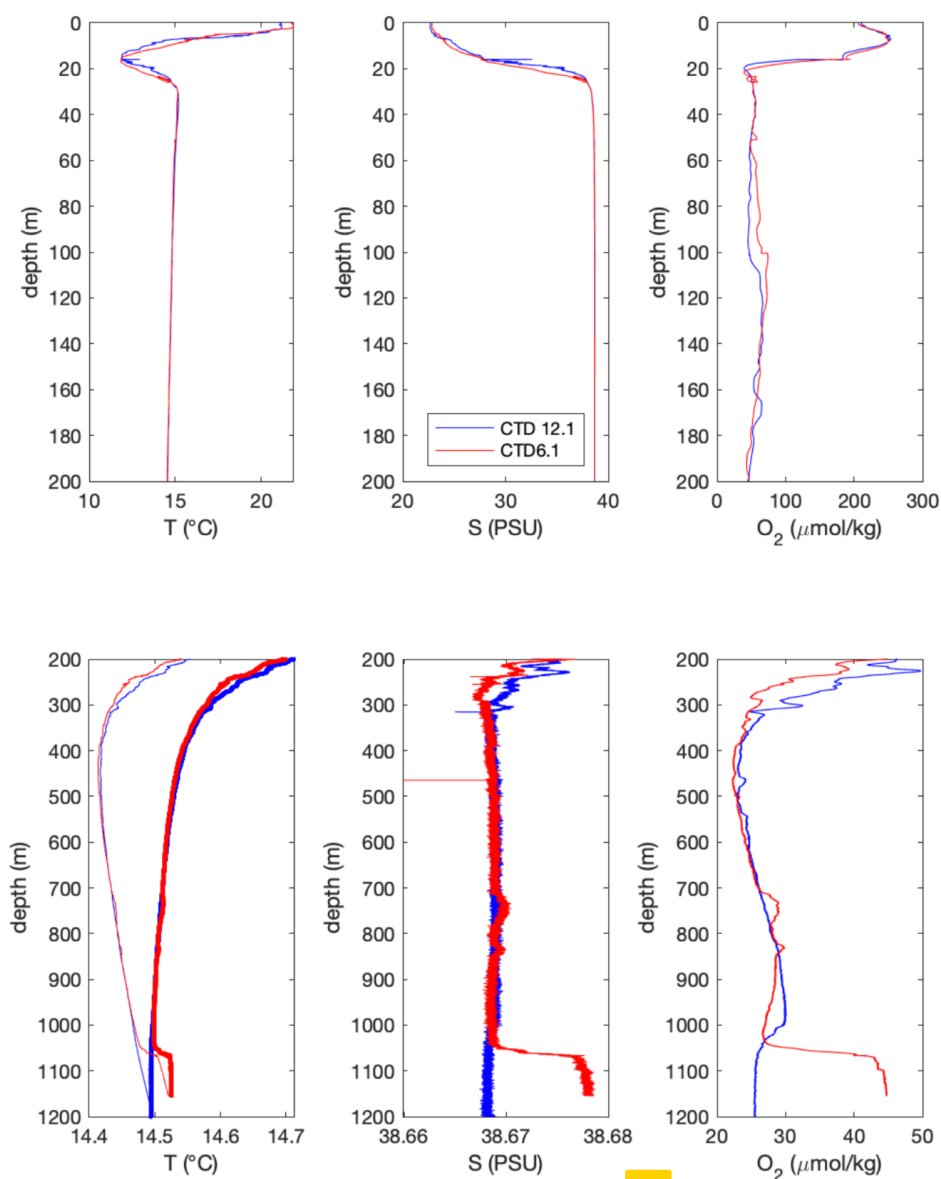
### 3.4. Temperature record

The Sea of Marmara is stratified, with a low salinity (20-22‰) 20-30 m surface layer that displays strong seasonal temperature variability overlaying a high salinity (about 38‰) body of seawater at 14-15°C derived from the Aegean Sea (Beşiktepe et al., 1994). Within this body, the potential temperature generally decreases with depth, which would in principle imply that a turbidity current, flowing downward, should cause a small temperature increase. However, the deployment site is prone to seasonal cascading, so that the initial temperature structure may have been disturbed. Example of CTD profiles recorded in June 2007 (Henry et al., 2007) are shown in Figure 8. No CTD profile is available in Sept 2019, but variations in temperature and oxygen concentration associated with mild currents (<5 cm/s) were recorded by the instrument in May-July 2019, and again on Sept 20.

Temperature variations associated with the  $M_w$  4.7 09/24/2019 earthquakes are very small, less than  $\pm 0.002^\circ\text{C}$ , which confirms that water did not travel far during this event. After the  $M_w$  5.8 09/26/2019 earthquake, the recorded temperature decreases progressively by about  $0.015^\circ\text{C}$ , after the first hydrologic disturbance and tilting of the instrument, until the recorded current reaches its maximum value (Figure 5). Temperature then progressively increases to reach nearly the same value as before the event. The small variation in temperature recorded indicates that the turbid water originates from the deep-water body. The slight temperature decrease observed after the earthquake can result from the mixing of a warmer bottom water layer with the bulk of the deep-water layer. However, the observation of a temperature drop precludes that the turbid water originates from depths less than 400 m, as water present between 400 m and the halocline is at a higher potential temperature than the deeper water throughout the year (see Beşiktepe et al., 1994, and figure 8). Moreover, an inflow of



412 water from closer to the surface should result in an increase in the O<sub>2</sub> concentration in  
 413 the bottom water, but none is observed in the data.  
 414



415  
 416 **Figure 8.** Depth plots of Temperature (°C), Salinity (PSU) and oxygen concentration  
 417 (μmol/kg) from CTD profiles acquired in the Sea of Marmara during Marnaut cruise of  
 418 Ifremer RV L'Atalante (Henry et al., 2007). On the lower temperature plot, thin lines



419 are measured values and thick lines are potential temperatures calculated at 1180 m.  
 420 Locations are shown on Figure 1

421

### 422 3.5. Inferred sequence of events

423 These observations provide some insight on the complex sequence of events  
 424 that followed the earthquake and suggest the following scenario. After the  $M_w$  4.7  
 425 09/24/2019 a turbid cloud formed east of the instrument and drifted slowly. Considering  
 426 the maximum velocity of the current (less than 4 cm/s) and the 4-hours interval  
 427 between the earthquake and the passing of the turbid cloud over the instrument, the  
 428 front of turbid water should have formed ENE of the instrument at a maximum distance  
 429 of about 500 m, and this coincides with the base of the northern slope near the outlet  
 430 of the canyon. It is suspected that instability on the steeper slopes on the sides of the  
 431 canyon is the primary cause of sediment suspension. The clouds subsequently drifted  
 432 downslope over a total horizontal distance of at most 1 kilometers before dissipating,  
 433 adding the 500 m estimate above to the drift calculated after the passing of the front  
 434 over the instrument (Figure 6).

435 The  $M_w$  5.8 09/26/1919 caused much stronger currents. After the passing of  
 436 the seismic wave, triggering of instability on slopes adjacent to the deployment site  
 437 caused mudflows that spread on the basin floor causing the tilting of the instrument  
 438 25 minutes after the earthquake, and bottom water turbidity. As the base of the nearest  
 439 slope is about 400 m north of the instrument, this would imply a minimum velocity of  
 440 20 cm/s for the mudflow to reach the device location in 25 minutes. During the following  
 441 10 hours, the current record is incomplete but indicates variations in strength and  
 442 direction. Widespread slope instabilities triggered by the earthquake may have resulted  
 443 in several turbidity currents recorded as successive pulses. The role of seiches and  
 444 surface gravity waves in sediment resuspension can be ruled out as no tsunami was  
 445 recorded by near shore tidal gauges around the Sea of Marmara. The relationship  
 446 between gravity wave amplitude  $A$  and bottom current amplitude  $U$  in the shallow water  
 447 linear approximation is given by  $U=(g/H)^{1/2}A$ , where  $H$  is water column height. An  
 448 oscillatory current of 10 cm/s at 1200 m depth would thus correspond to a free surface  
 449 oscillation of 1 m (or 100 hPa) for a standing wave (seiche) as well as a progressive  
 450 wave (tsunami). This should have been easily detected in a sea where tidal amplitude  
 451 is about 10 cm (Alpar and Yüce, 1998). The influence of baroclinic internal waves on



the halocline at 20-30 m depth must also be ruled out as they cannot physically produce currents of more than a few cm/s at 1200 m. However, It remains possible that the interface at the top of the turbid cloud is affected by baroclinic waves. The strongest current is recorded after 10 hours, which suggests that a turbidity current initiated further upslope may have reached the site after a longer delay but may also have gained more kinetic energy on its downhill path. This event, reaching a speed exceeding 25 cm/s apparently caused enough erosion to free the device from the mud accumulation. The current then stabilizes in a westward direction and decays progressively over the next 9 hours, which suggests the tail of a turbidity current flowing in the canyon E of the deployment site has been recorded. The hours-long delay between the earthquake and the passing of the fastest current over the instrument may hypothetically correspond to the time for the head of the turbidity current to travel from its source to the location of the instrument. The length of the canyon valley between the device location and the 400 m isobath, inferred to be the minimum depth of the turbid water source, is about 13 km. In this scenario, the average velocity of the head of the turbidity current would be 30-40 cm/s. Alternatively, a sequence of slope failures may have lasted up to several hours after the earthquake. The distance travelled by the turbidity current on the basin floor beyond the instrument may be estimated from the calculated drift during the waing phase, and is found to be about 5 km (Figure 6). When plotted over the bathymetric map the drift appears to stay within the depositional fan at the outlet of the canyon, the extension of which is known from sediment sounder profiles (Figure 1). These calculations are only a rough estimate of the distance travelled by suspended particles as only the velocity at 1.5 m above the seafloor is known. However, it appears unlikely that sediments spread all over the 15x20 km basin floor as this would require velocities of the order of 1m/s, sustained over a wide area for several hours.

The decay of the backscatter signal strength over the next 3 days may reflect the settling of sand size particles put in suspension in the water column after this sequence of events. For a first order assessment, Stokes settling velocity, an upper bound valid in dilute suspensions (e.g. Guazelli and Morris, 2012) may be used. The Stokes settling velocity of 63  $\mu\text{m}$  quartz grains (density 2650 kg/m<sup>3</sup>) in 13°C seawater is 2.7 mm/s, allowing such grains to drop by 700 m in 3 days. However, if the particles forming the cloud are mostly composed of clay aggregates, which density may be comprised between 1200 and 1700 kg/m<sup>3</sup>, the settling velocity would be comprised



486 between 0.3 mm and 1 mm/s. In this case the height of the suspended particle cloud  
 487 could range between 70 and 250 m.

#### 488 4. Discussion and conclusion

489 Data obtained with a seafloor device located at the outlet of a canyon in the  
 490 Central Basin in the Sea of Marmara bring some insight on how earthquakes scale  
 491 with their hydrodynamic consequences. In September 2019,  $M_w$  4.7 and 5.8  
 492 earthquakes occurred at a 5 km distance from the device as well as a series of smaller  
 493 foreshocks and aftershocks. In this setting, earthquakes of magnitude less than 4 did  
 494 not cause noticeable water column turbidity nor currents. The  $M_w$  4.7 earthquake  
 495 generated a turbid cloud on slopes a few hundred meters from the instrument and the  
 496 cloud took 3–4 hours to drift down to the instrument location and 10 more hours to  
 497 dissipate. As the current velocity remained small (less than 4 cm/s), it can be concluded  
 498 that this cloud did not evolve into a self-sustained turbidity current (Parker, 1982).  
 499  $M_w$  5.8 earthquake initiated a turbidity current and the data obtained may be compared  
 500 with more complete records of turbidity currents obtained elsewhere with ADCP  
 501 deployments and/or water column mooring lines. The duration of the event in the Sea  
 502 of Marmara (about 10 hours) appear fairly typical and comparable with events recorded  
 503 in other locations regardless of the initiation mechanism, which comprise hyperpycnal  
 504 flows from river floods (Var and Gaoping canyons), storm waves and dredging (Gulf of  
 505 St. Lawrence and Monterey canyon), and slope instabilities triggered by an earthquake  
 506 (Tokachi-oki) or by other processes (Var canyon) (Normandeau et al., 2019;  
 507 Khripounoff et al., 2012; Xu et al., 2004; Liu et al., 2012; Mikada et al., 2006). Longer  
 508 duration events with very different hydrodynamic characteristics have been observed  
 509 in larger scale systems (e.g. Congo deep sea canyon, Azpiroz-Zabala et al., 2017). On  
 510 the other hand, events recorded closer to shore on the edge of the continental shelf or  
 511 on a delta front have much shorter durations (Xu et al., 2010; Hughes Clarke, 2016).  
 512 In events of comparable scale to the Sea of Marmara one, the velocity of the current  
 513 generally reaches its maximum several meters above the seafloor, so that the velocity  
 514 recorded by our instrument at 1.5 m from the seafloor is within the boundary layer, and  
 515 lower than either the maximum current velocity or the velocity of the head of the  
 516 turbidity current. A velocity of several tens of centimeter per second is representative  
 517 of the slower recorded examples, corresponding to mud rich flows associated with  
 518 hyperpycnal flows, the smaller landslides (Khripounoff et al. 2012) or to the smaller





storm-related events (Normandeau et al., 2019). Turbidites following large earthquakes or large slope instabilities have reached maximum velocities of 20 m/s (Piper et al., 1999). Velocities of 2-7 m/s were reported for the turbidity current following Tohoku earthquake (Arai et al., 2013) and 1.4 m/s in the Tokachi-Oki case (Mikada et al., 2006). The downward current after the off-Izu Peninsula earthquake may be constrained with a noisy ADCP record to a maximum of 10-15 cm/s in a 20-30 m layer above the seafloor and lasted about one hour, peaking about 30 minutes after the earthquake (Kasaya et al., 2009). This turbidity current thus appears less intense and shorter in duration than the one recorded in the Sea of Marmara, but the triggering earthquake was also smaller (M5.4 compared to M5.8) and more distant (10 km). These observations suggest that a general scaling relationship could exist between earthquake magnitudes and the strength and extent of the turbidity currents they induce. Moreover, although the off-Izu event is shorter than the Sea of Marmara one, they share an important characteristic in that the turbid cloud is observed to form when a mud flow hits the observatory site and some time before current builds up in the water column.

The 10 hours delay observed in the Sea of Marmara between the triggering event and the peak of the turbidity current is long compared to the 2 hours delay observed after Tohoku and Tokachi-oki earthquakes. We suggested earlier that the long delay may simply result from a slower velocity of the turbidity current or from delayed slope failure. Another possibility is delayed ignition, which may occur if the turbidity current develops indirectly from the hydrodynamic instability of a turbid cloud resulting from slope failures and/or ground shaking rather than by acceleration of a dense mud flow (Parker, 1982; Mulder and Cochonnat, 1996; Piper and Normark, 2009).

The scenario we propose for the Sept 26, 2019 earthquake involving mud flows from proximal sources, followed by turbidity currents originating at larger distances, and the subsequent settling of sediment in suspension, could relate with the structure of turbidite-homogenites. Progressive or pulsed build-up of turbidity current energy is considered typical of hyperpycnal flows initiated by river floods (Mulder et al., 2003) but reverse grading and pulsing is also observed in seismic turbidites (Gutierrez-Pastor et al., 2013). In the Sea of Marmara, many of the laminated turbidites sampled in Kumburgaz Basin formed from the amalgamation (below the homogenite layer) of at least two flows, the first one being finer and less sorted (Yakupoglu et al., 2019). The



553 coarsening observed in this context is often associated with an increase of the calcium  
 554 content indicative of a shallower source, rich in biogenic carbonate material. However,  
 555 in the case observed in the present study, remobilization of sediment should be limited  
 556 to the lower slope as the temperature of the displaced water precludes a source  
 557 shallower than 400 m water depth.

558 The geomorphological context of the deployment site south of a slope identified  
 559 as unstable from geomorphological criteria (Zitter et al., 2012), and on a depositional  
 560 fan at the outlet of a canyon is also consistent with the proposed scenario. We  
 561 estimated by integrating recorded current velocity that the current during this event  
 562 was not strong enough to spread the sediment over the entire Central Basin floor but  
 563 that the zone of deposition was probably comparable in size to the fan. It can be  
 564 inferred that the paleoseismological record from a core taken in the fan should contain  
 565 more events than one taken at the basin depocenter. A sediment sounder profile  
 566 (Figure 1) also shows that the character of the seismic reflectors differs in the basin  
 567 and in the fan and that establishing reliable correlations between them is not simple.  
 568 However, as hypothesized by previous studies (McHugh et al., 2014), turbidite-  
 569 homogenite deposits that can be correlated between cores taken at various locations  
 570 in the basin probably correspond to the larger events, which may be correlated with  
 571 historical earthquakes. Moreover, it is still unknown whether the Sept 26 event left a  
 572 trace on the seafloor morphology and in the sediment record. Performing new core  
 573 sampling and very high-resolution geophysical surveys in this area would thus have  
 574 important implications for the understanding of seismoturbidite records and for the  
 575 assessment of geohazards.

576

## 577 Acknowledgements

578 Financial support was provided by the bilateral ANR/TÜBITAK collaborative research  
 579 project MAREGAMI (ANR-16-CE03-0010-02 and Tübitak Project 116Y371) and by  
 580 CNRS-INSU through the European Multidisciplinary Sea Observatory (EMSO)  
 581 Research Infrastructure program. DT-INSU and Istanbul Technical University  
 582 hydrodynamic engineering department provided technical support for device design,  
 583 construction, and deployment. Bernard Mercier de Lépinay provided processed  
 584 sediment sounder profiles. We thank the crew and Captain of R/V Yunus (Istanbul  
 585 University) for their support during installation and recovery of the instruments.



586 Seafloor monitoring data are available through SEANOE (Henry et al., 2021) and  
 587 CTD profile data through SISMER Oceanographic Data portal (Henry et al., 2007).  
 588

## 589 References

- 590 Alpar, B., & Yüce, H. (1998). Sea-level variations and their interactions between the Black  
 591 Sea and the Aegean Sea. *Estuarine, Coastal and Shelf Science*, 46, 609–619.
- 592 Arai, K., Naruse, H., Miura, R., Kawamura, K., Hino, R., Ito, Y., Inazu, D., Yokokawa, M.,  
 593 Izumi, N., Murayama, M., & Kasaya, T. (2013). Tsunami-generated turbidity current of  
 594 the 2011 Tohoku-Oki earthquake. *Geology*, 41(11), 1195–1198.  
 595 <https://doi.org/10.1130/G34777.1>
- 596 Armijo, R., Meyer, B., Navarro, S., King, G., & Barka, A. (2002). Asymmetric slip partitioning  
 597 in the Sea of Marmara pull-apart: a clue to propagation processes of the North Anatolian  
 598 Fault? *Terra Nova*, 14(2), 80–86. <https://doi.org/10.1046/j.1365-3121.2002.00397.x>
- 599 Armijo, R. and J. Malavieille (2002) MARMARASCARPS cruise, RV L'Atalante,  
 600 <https://doi.org/10.17600/2010140>
- 601 Azpiroz-Zabala, M., Cartigny, M. J. B., Talling, P. J., Parsons, D. R., Sumner, E. J., Clare, M.  
 602 A., Simmons, S. M., Cooper, C., & Pope, E. L. (2017). Newly recognized turbidity current  
 603 structure can explain prolonged flushing of submarine canyons. *Science Advances*,  
 604 3(10). <https://doi.org/10.1126/sciadv.1700200>
- 605 Beck, C., Mercier de Lépinay, B., Schneider, J. L., Cremer, M., Çağatay, N., Wendenbaum,  
 606 E., et al. (2007). Late Quaternary co-seismic sedimentation in the Sea of Marmara's  
 607 deep basins. *Sedimentary Geology*, 199, 65–89.  
 608 <https://doi.org/10.1016/j.sedgeo.2005.12.031>
- 609 Beşiktepe, Ş. T., Sur, H. İ., Özsoy, E., Latif, M. A., Oğuz, T., & Ünlüata, Ü. (1994). The  
 610 circulation and hydrography of the Marmara Sea. *Progress in Oceanography*, 34(4),  
 611 285–334. [https://doi.org/10.1016/0079-6611\(94\)90018-3](https://doi.org/10.1016/0079-6611(94)90018-3)
- 612 Brizuela, N., Filonov, A., & Alford, M. H. (2019). Internal tsunami waves transport sediment  
 613 released by underwater landslides. *Scientific Reports*, 9(1), 10775.  
 614 <https://doi.org/10.1038/s41598-019-47080-0>
- 615 Bulut, F., Aktuğ, B., Yaltırak, C., Doğru, A., & Özener, H. (2019). Magnitudes of future large  
 616 earthquakes near Istanbul quantified from 1500 years of historical earthquakes, present-  
 617 day microseismicity and GPS slip rates. *Tectonophysics*, 764(July 2018), 77–87.  
 618 <https://doi.org/10.1016/j.tecto.2019.05.005>
- 619 Çağatay, M. N., Erel, L., Bellucci, L. G., Polonia, a., Gasperini, L., Eriş, K. K., Sancar, Ü.,  
 620 Biltekin, D., Uçarkuş, G., Ülgen, U. B., & Damci, E. (2012). Sedimentary earthquake



- 621 records in the İzmit Gulf, Sea of Marmara, Turkey. *Sedimentary Geology*, 282, 347–359.  
622 <https://doi.org/10.1016/j.sedgeo.2012.10.001>
- 623 Çağatay, N. M., Uçarkus, G., Eris, K. K., Henry, P., Gasperini, L., & Polonia, A. (2015).  
624 Submarine canyons of the Sea of Marmara. In F. Briand (Ed.), *Submarine Canyon*  
625 *Dynamics in the Mediterranean and Tributary Seas*, CIESM Workshop Monograph n° 47  
626 (pp. 123–135). CIESM Publisher, Monaco. <https://doi.org/10.13140/RG.2.1.1692.8402>
- 627 Cattaneo, A., Babonneau, N., Ratzov, G., Dan-Unterseh, G., Yelles, K., Bracane, R., Mercier  
628 De Lapinay, B., Boudiaf, A., & Daverchare, J. (2012). Searching for the seafloor  
629 signature of the 21 May 2003 Boumerdas earthquake offshore central Algeria. *Natural*  
630 *Hazards and Earth System Science*, 12(7), 2159–2172. [https://doi.org/10.5194/nhess-](https://doi.org/10.5194/nhess-12-2159-2012)  
631 [12-2159-2012](https://doi.org/10.5194/nhess-12-2159-2012)
- 632 Dan, G., Sultan, N., Savoye, B., Deverchere, J., & Yelles, K. (2009). Quantifying the role of  
633 sandy-silty sediments in generating slope failures during earthquakes: Example from the  
634 Algerian margin. *International Journal of Earth Sciences*, 98(4), 769–789.  
635 <https://doi.org/10.1007/s00531-008-0373-5>
- 636 Drab, L., Hubert Ferrari, A., Schmidt, S., & Martinez, P. (2012). The earthquake sedimentary  
637 record in the western part of the Sea of Marmara, Turkey. *Natural Hazards and Earth*  
638 *System Science*, 12(4), 1235–1254. <https://doi.org/10.5194/nhess-12-1235-2012>
- 639 Drab, L., Hubert-Ferrari, A., Schmidt, S., Martinez, P., Carlut, J., & El Ouahabi, M. (2015).  
640 Submarine Earthquake History of the Çınarcık Segment of the North Anatolian Fault in  
641 the Marmara Sea, Turkey. *Bulletin of the Seismological Society of America*, 105(2A),  
642 622–645. <https://doi.org/10.1785/0120130083>
- 643 Eriş, K. K., Çağatay, N., Beck, C., Mercier de Lepinay, B., & Corina, C. (2012). Late-  
644 Pleistocene to Holocene sedimentary fills of the Çınarcık Basin of the Sea of Marmara.  
645 *Sedimentary Geology*, 281, 151–165. <https://doi.org/10.1016/j.sedgeo.2012.09.001>
- 646 Garfield, N., Rago, T. A., Schnebele, K. J., & Collins, C. A. (1994). Evidence of a turbidity  
647 current in Monterey Submarine Canyon associated with the 1989 Loma Prieta  
648 earthquake. *Continental Shelf Research*, 14(6), 673–686. [https://doi.org/10.1016/0278-](https://doi.org/10.1016/0278-4343(94)90112-0)  
649 [4343\(94\)90112-0](https://doi.org/10.1016/0278-4343(94)90112-0)
- 650 Goldfinger, C., Nelson, C. H., & Johnson, J. E. (2003). Holocene earthquake records from  
651 the cascadia subduction zone and northern san andreas fault based on precise dating of  
652 offshore turbidites. *Annual Review of Earth and Planetary Sciences*, 31(1), 555–577.  
653 <https://doi.org/10.1146/annurev.earth.31.100901.141246>
- 654 Goldfinger, C., Nelson, C. H., Morey, A. E., Johnson, J. E., Patton, J., Karabanov, E.,  
655 Gutiérrez-Pastor, J., Eriksson, A. T., Gràcia, E., Dunhill, G., Enkin, R. J., Dallimore, A., &  
656 Vallier, T. (2012). Earthquake Hazards of the Pacific Northwest Coastal and Marine  
657 Regions Turbidite Event History — Methods and Implications for Holocene



- 658 Paleoseismicity of the Cascadia Subduction Zone Professional Paper 1661 – F. USGS,  
659 Professional Paper 1661-F, 170. Retrieved from <http://pubs.usgs.gov/pppp1661f/>  
660 Grall, C., Henry, P., Tezcan, D., Mercier de Lepinay, B., Becel, A., Geli, L., Rudkiewicz, J.-L.,  
661 Zitter, T., & Harnegnies, F. (2012). Heat flow in the Sea of Marmara Central Basin:  
662 Possible implications for the tectonic evolution of the North Anatolian fault. *Geology*,  
663 40(1), 3–6. <https://doi.org/10.1130/G32192.1>  
664 Guazzelli, E., Morris, J. F., & Pic, S. (2011). *A Physical Introduction to Suspension*  
665 *Dynamics*. Cambridge: Cambridge University Press.  
666 <https://doi.org/10.1017/CBO9780511894671>  
667 Guerrero, M., Rüther, N., & Szupiany, R. N. (2012). Laboratory validation of acoustic Doppler  
668 current profiler (ADCP) techniques for suspended sediment investigations. *Flow*  
669 *Measurement and Instrumentation*, 23(1), 40–48.  
670 <https://doi.org/10.1016/j.flowmeasinst.2011.10.003>  
671 Guerrero, M., Szupiany, R. N., & Amsler, M. (2011). Comparison of acoustic backscattering  
672 techniques for suspended sediments investigation. *Flow Measurement and*  
673 *Instrumentation*, 22(5), 392–401. <https://doi.org/10.1016/j.flowmeasinst.2011.06.003>  
674 Gutiérrez-Pastor, J., Nelson, C. H., Goldfinger, C., & Escutia, C. (2013). Sedimentology of  
675 seismo-turbidites off the Cascadia and northern California active tectonic continental  
676 margins, northwest Pacific Ocean. *Marine Geology*, 336, 99–119.  
677 <https://doi.org/10.1016/j.margeo.2012.11.010>  
678 Hébert, H., Schindelé, F., Altinok, Y., Alpar, B., & Gazioglu, C. (2005). Tsunami hazard in the  
679 Marmara Sea (Turkey): A numerical approach to discuss active faulting and impact on  
680 the Istanbul coastal areas. *Marine Geology*, 215, 23–43.  
681 <https://doi.org/10.1016/j.margeo.2004.11.006>  
682 Heezen, B. C., Ericson, D. B., & Ewing, M. (1954). Further evidence for a turbidity current  
683 following the 1929 Grand banks earthquake. *Deep Sea Research* (1953), 1(4), 193–202.  
684 [https://doi.org/10.1016/0146-6313\(54\)90001-5](https://doi.org/10.1016/0146-6313(54)90001-5)  
685 Henry, P., A.M.C. Şengör, M.N. Çağatay (2007) MARNAUT cruise, RV L'Atalante,  
686 <https://doi.org/10.17600/7010070>  
687 Henry, P., Özeren M.S., Desprez De Gesincourt O., de Saint-Leger E., Libes, M., Çakir, Z.,  
688 Yakupoğlu, N., Géli, L. (2021). EMSO / MAREGAMI Marmara bottom pressure and  
689 current records. SEANO. <https://doi.org/10.17882/78928>  
690 Hsu, S. K., Kuo, J., Lo, C. L., Tsai, C. H., Doo, W. Bin, Ku, C. Y., & Sibuet, J. C. (2008).  
691 Turbidity currents, submarine landslides and the 2006 Pingtung earthquake off SW  
692 Taiwan. *Terrestrial, Atmospheric and Oceanic Sciences*, 19(6), 767–772.  
693 [https://doi.org/10.3319/TAO.2008.19.6.767\(PT\)](https://doi.org/10.3319/TAO.2008.19.6.767(PT))



- 694 Hughes Clarke, J. E. (2016). First wide-angle view of channelized turbidity currents links  
695 migrating cyclic steps to flow characteristics. *Nature Communications*, 7(1), 11896.  
696 <https://doi.org/10.1038/ncomms11896>
- 697 Ikehara, K., Kanamatsu, T., Nagahashi, Y., Strasser, M., Fink, H., Usami, K., et al. (2016).  
698 Documenting large earthquakes similar to the 2011 Tohoku-oki earthquake from  
699 sediments deposited in the Japan Trench over the past 1500 years. *Earth and Planetary*  
700 *Science Letters*, 445, 48–56. doi:10.1016/j.epsl.2016.04.009
- 701 Karabulut, H., Güvercin, S. E., Eskikoç, F., Konca, A. Ö., & Ergintav, S. (2021). The  
702 moderate size 2019 September Mw5.8 Silivri earthquake unveils the complexity of the  
703 Main Marmara Fault shear zone. *Geophysical Journal International*, 224(1), 377–388.  
704 <https://doi.org/10.1093/gji/ggaa469>
- 705 Kasaya, T., Mitsuzawa, K., Goto, T., Iwase, R., Sayanagi, K., Araki, E., Asakawa, K., Mikada,  
706 H., Watanabe, T., Takahashi, I., & Nagao, T. (2009). Trial of Multidisciplinary  
707 Observation at an Expandable Sub-Marine Cabled Station “Off-Hatsushima Island  
708 Observatory” in Sagami Bay, Japan. *Sensors*, 9(11), 9241–9254.  
709 <https://doi.org/10.3390/s91109241>
- 710 Khripounoff, A., Crassous, P., Lo Bue, N., Dennielou, B., & Silva Jacinto, R. (2012). Different  
711 types of sediment gravity flows detected in the Var submarine canyon (northwestern  
712 Mediterranean Sea). *Progress in Oceanography*, 106, 138–153.  
713 <https://doi.org/10.1016/j.pocean.2012.09.001>
- 714 Le Pichon, X., Chamot-Rooke, N., Rangin, C., & Sengör, A. M. C. (2003). The North  
715 Anatolian fault in the Sea of Marmara. *Journal of Geophysical Research*, 108, 2179.  
716 <https://doi.org/10.1029/2002JB001862>
- 717 Le Pichon, X., Şengör, A. M. C., Demirbağ, E., Rangin, C., İmren, C., Armijo, R., Görür, N.,  
718 Çağatay, N., Mercier de Lepinay, B., Meyer, B., Saatçılar, R., & Tok, B. (2001). The  
719 active Main Marmara Fault. *Earth and Planetary Science Letters*, 192(4), 595–616.  
720 [https://doi.org/10.1016/S0012-821X\(01\)00449-6](https://doi.org/10.1016/S0012-821X(01)00449-6)
- 721 Liu, J. T., Wang, Y.-H., Yang, R. J., Hsu, R. T., Kao, S.-J., Lin, H.-L., & Kuo, F. H. (2012).  
722 Cyclone-induced hyperpycnal turbidity currents in a submarine canyon. *Journal of*  
723 *Geophysical Research: Oceans*, 117(C4), n/a-n/a.  
724 <https://doi.org/10.1029/2011JC007630>
- 725 McHugh, C. M. G., Seeber, L., Cormier, M. H., Dutton, J., Cagatay, N., Polonia, A., Ryan, W.  
726 B. F., & Gorur, N. (2006). Submarine earthquake geology along the North Anatolia Fault  
727 in the Marmara Sea, Turkey: A model for transform basin sedimentation. *Earth and*  
728 *Planetary Science Letters*, 248, 661–684. <https://doi.org/10.1016/j.epsl.2006.05.038>
- 729 McHugh, C. M., Seeber, L., Braudy, N., Cormier, M. H., Davis, M. B., Diebold, J. B.,  
730 Dieudonne, N., Douilly, R., Gulick, S. P. S., Hornbach, M. J., Johnson, H. E., Mishkin, K.





- 731 R., Sorlien, C. C., Steckler, M. S., Symithe, S. J., & Templeton, J. (2011). Offshore  
 732 sedimentary effects of the 12 January 2010 Haiti earthquake. *Geology*, 39(8), 723–726.  
 733 <https://doi.org/10.1130/G31815.1>
- 734 McHugh, C. M. G., Braudy, N., Çağatay, M. N., Sorlien, C., Cormier, M.-H., Seeber, L., &  
 735 Henry, P. (2014). Seafloor fault ruptures along the North Anatolia Fault in the Marmara  
 736 Sea, Turkey: Link with the adjacent basin turbidite record. *Marine Geology*, 353, 65–83.  
 737 <https://doi.org/10.1016/j.margeo.2014.03.005>
- 738 Mikada, H., Mitsuzawa, K., Matsumoto, H., Watanabe, T., Morita, S., Otsuka, R., Sugioka,  
 739 H., Baba, T., Araki, E., & Suyehiro, K. (2006). New discoveries in dynamics of an M8  
 740 earthquake-phenomena and their implications from the 2003 Tokachi-oki earthquake  
 741 using a long term monitoring cabled observatory. *Tectonophysics*, 426(1–2), 95–105.  
 742 <https://doi.org/10.1016/j.tecto.2006.02.021>
- 743 Mulder, T., & Cochonnat, P. (1996). Classification of Offshore Mass Movements. *SEPM*  
 744 *Journal of Sedimentary Research*, Vol. 66. [https://doi.org/10.1306/D42682AC-2B26-](https://doi.org/10.1306/D42682AC-2B26-11D7-8648000102C1865D)  
 745 [11D7-8648000102C1865D](https://doi.org/10.1306/D42682AC-2B26-11D7-8648000102C1865D)
- 746 Mulder, T., Syvitski, J. P. M., Migeon, S., Faugères, J.-C., & Savoye, B. (2003). Marine  
 747 hyperpycnal flows: initiation, behavior and related deposits. A review. *Marine and*  
 748 *Petroleum Geology*, 20(6–8), 861–882. <https://doi.org/10.1016/j.marpetgeo.2003.01.003>
- 749 Nakajima, T., & Kanai, Y. (2000). Sedimentary features of seismoturbidites triggered by the  
 750 1983 and older historical earthquakes in the eastern margin of the Japan Sea.  
 751 *Sedimentary Geology*, 135(1–4), 1–19. [https://doi.org/10.1016/S0037-0738\(00\)00059-2](https://doi.org/10.1016/S0037-0738(00)00059-2)
- 752 Normandeau, A., Bourgault, D., Neumeier, U., Lajeunesse, P., St-Onge, G., Gostiaux, L., &  
 753 Chavanne, C. (2020). Storm-induced turbidity currents on a sediment-starved shelf:  
 754 Insight from direct monitoring and repeat seabed mapping of upslope migrating  
 755 bedforms. *Sedimentology*, 67(2), 1045–1068. <https://doi.org/10.1111/sed.12673>
- 756 Okal, E. A., & Synolakis, C. E. (2001). Comment on “Origin of the 17 July 1998 Papua New  
 757 Guinea Tsunami: Earthquake or Landslide?” by E. L. Geist. *Seismological Research*  
 758 *Letters*, 72(3), 362–366. <https://doi.org/10.1785/gssrl.72.3.362>
- 759 Özeren, M. S., Çağatay, M. N., Postacioğlu, N., Şengör, a. M. C., Görür, N., & Eriş, K.  
 760 (2010). Mathematical modelling of a potential tsunami associated with a late glacial  
 761 submarine landslide in the Sea of Marmara. *Geo-Marine Letters*, 30, 523–539.  
 762 <https://doi.org/10.1007/s00367-010-0191-1>
- 763 Parker, G. (1982). Conditions for the ignition of catastrophically erosive turbidity currents.  
 764 *Marine Geology*, 46(3–4), 307–327. [https://doi.org/10.1016/0025-3227\(82\)90086-X](https://doi.org/10.1016/0025-3227(82)90086-X)
- 765 Piper, D. J. W., & Normark, W. R. (2009). Processes That Initiate Turbidity Currents and  
 766 Their Influence on Turbidites: A Marine Geology Perspective. *Journal of Sedimentary*  
 767 *Research*, 79(6), 347–362. <https://doi.org/10.2110/jsr.2009.046>



- 768 Piper, D. J. W., Cochonat, P., & Morrison, M. L. (1999). The sequence of events around the  
769 epicentre of the 1929 Grand Banks earthquake: initiation of debris flows and turbidity  
770 current inferred from sidescan sonar. *Sedimentology*, 46(1), 79–97.  
771 <https://doi.org/10.1046/j.1365-3091.1999.00204.x>
- 772 Polonia, A., Vaiani, S. C., & De Lange, G. J. (2016). Did the A.D. 365 Crete  
773 earthquake/tsunami trigger synchronous giant turbidity currents in the Mediterranean  
774 Sea? *Geology*, 44(3), 191–194. <https://doi.org/10.1130/G37486.1>
- 775 Pope, E. L., Talling, P. J., & Carter, L. (2017). Which earthquakes trigger damaging  
776 submarine mass movements: Insights from a global record of submarine cable breaks?  
777 *Marine Geology*, 384, 131–146. <https://doi.org/10.1016/j.margeo.2016.01.009>
- 778 Şengör, A. M. C., Grall, C., İmren, C., Le Pichon, X., Görür, N., Henry, P., Karabulut, H., &  
779 Siyako, M. (2014). The geometry of the North Anatolian transform fault in the Sea of  
780 Marmara and its temporal evolution: implications for the development of intracontinental  
781 transform faults. *Canadian Journal of Earth Sciences*, 51(3), 222–242.  
782 <https://doi.org/10.1139/cjes-2013-0160>
- 783 Synolakis, C. E., Bardet, J.-P., Borrero, J. C., Davies, H. L., Okal, E. A., Silver, E. A., Sweet,  
784 S., & Tappin, D. R. (2002). The slump origin of the 1998 Papua New Guinea Tsunami.  
785 *Proceedings of the Royal Society of London. Series A: Mathematical, Physical and*  
786 *Engineering Sciences*, 458(2020), 763–789. <https://doi.org/10.1098/rspa.2001.0915>
- 787 Xu, J. P., Noble, M. A., & Rosenfeld, L. K. (2004). In-situ measurements of velocity structure  
788 within turbidity currents. *Geophysical Research Letters*, 31(9).  
789 <https://doi.org/10.1029/2004GL019718>
- 790 Xu, J. P., Swarzenski, P. W., Noble, M., & Li, A.-C. (2010). Event-driven sediment flux in  
791 Hueneme and Mugu submarine canyons, southern California. *Marine Geology*, 269(1–  
792 2), 74–88. <https://doi.org/10.1016/j.margeo.2009.12.007>
- 793 Yakupoğlu, N., Uçarkuş, G., Kadir Eriş, K., Henry, P., & Namık Çağatay, M. (2019).  
794 Sedimentological and geochemical evidence for seismoturbidite generation in the  
795 Kumburgaz Basin, Sea of Marmara: Implications for earthquake recurrence along the  
796 Central High Segment of the North Anatolian Fault. *Sedimentary Geology*, 380, 31–44.  
797 <https://doi.org/10.1016/j.sedgeo.2018.11.002>
- 798 Zitter, T. A. C., Grall, C., Henry, P., Özeren, M. S., Çağatay, M. N., Şengör, A. M. C.,  
799 Gasperini, L., de Lépinay, B. M., & Géli, L. (2012). Distribution, morphology and triggers  
800 of submarine mass wasting in the Sea of Marmara. *Marine Geology*, 329–331, 58–74.  
801 <https://doi.org/10.1016/j.margeo.2012.09.002>